

Efficient Implementation of Ab Initio Quantum Embedding in Periodic Systems: Density Matrix Embedding Theory

Zhi-Hao Cui, Tianyu Zhu, and Garnet Kin-Lic Chan*

*Division of Chemistry and Chemical Engineering, California Institute of Technology,
Pasadena, CA 91125, USA*

E-mail: gkc1000@gmail.com

Abstract

We describe an efficient quantum embedding framework for realistic *ab initio* density matrix embedding (DMET) calculations in solids. We discuss in detail the choice of orbitals and mapping to a lattice, treatment of the virtual space and bath truncation, and the lattice-to-embedded integral transformation. We apply DMET in this *ab initio* framework to a hexagonal boron nitride monolayer, crystalline silicon, and nickel monoxide in the antiferromagnetic phase, using large embedded clusters with up to 300 embedding orbitals. We demonstrate our formulation of *ab initio* DMET in the computation of ground-state properties such as the total energy, equation of state, magnetic moment and correlation functions.

1 Introduction

The *ab initio* description of strongly correlated electrons in solids is a major challenge, limiting the quantitative understanding of interacting electronic phases, such as the Mott¹

and high-temperature superconducting phases.²⁻⁴ The heart of the difficulty lies in the need to use computational methods that can treat correlated electrons, which usually means a steep computational scaling with system size, as well as treat the thermodynamic limit (TDL), in order to observe distinct phases.

A formal route to extend high-level correlated electron methods to infinite systems is provided by *quantum embedding*.^{5,6} While there are today a wide variety of techniques termed embedding,⁶ we will be concerned with the type of quantum embeddings in condensed phases that historically started with the treatment of defects in solids via the Anderson impurity model, where the interacting impurity site is surrounded by a set of bath orbitals that approximately represent the environment.⁷ This impurity idea can be generalized to translationally invariant systems, where the lattice is subdivided into multiple clusters (also termed impurities or fragments) where each is embedded in a self-consistent environment generated by the other impurities. In the embedding treatment, only the solution of the embedded cluster (i.e. the cluster along with its quantum bath) is treated by the high-level correlated method (the impurity solver), while interactions between clusters are treated at a lower level of theory, typically within a single-particle framework such as mean-field.

Dynamical mean-field theory (DMFT) was the first quantum embedding algorithm for periodic systems based on the above self-consistent quantum impurity idea,^{8,9} and has since been extended in many different directions and settings.⁹⁻¹⁷ DMFT is formulated in terms of the one-particle Green's function, and solving the embedded impurity problem yields a local self-energy that is then used in the single-particle Green's function description of the periodic lattice. More recently, density matrix embedding theory (DMET)¹⁸ has been proposed as a computationally simpler quantum embedding algorithm, also for a self-consistent quantum impurity, but adopting the one-particle reduced density matrix as the fundamental variable, in conjunction with a static mean-field description of the periodic lattice.¹⁸⁻²² Because DMET only requires to compute frequency-independent observables, it is less expensive than DMFT, and in practice, a wider variety of correlated electron methods can be applied to the impurity

problem. A further kind of quantum embedding, density functional (or wavefunction-in-density functional) embedding²³⁻³¹ is also of much current interest. However, this is not usually applied to strongly correlated phases, and thus we do not consider it further here.

In this work, we will focus our attention on the *ab initio* implementation of DMET in periodic solids. While DMET has been successfully applied to compute electronic phase diagrams across a range of strongly correlated lattice models,^{18-22,32-36} the extension of DMET to a practical *ab initio* method for periodic systems remains incomplete. There have been several works on cyclic H and Be ring structures³⁷⁻⁴⁰ and an early DMET implementation for solids that treated minimal unit cells and small basis sets⁴¹ (e.g. 2D boron nitride in the 6-31G basis and diamond in a STO-3G basis⁴¹). However, such calculations are best considered model *ab initio* calculations in the sense that the basis sets and impurity sizes are too small for quantitative or chemical accuracy. What remains to be developed is a comprehensive computational framework in periodic DMET calculations that can use both large and realistic basis sets, and treat non-trivial cluster sizes or complicated unit cells with many atoms. Describing such a framework is the purpose of the current work.

To establish a practical implementation of *ab initio* periodic DMET, it is worth outlining the similarities and differences between a calculation on a lattice model and a realistic solid. On the one hand, both models and real solids are translationally invariant over cells, and thus for an efficient computational algorithm, \mathbf{k} -point symmetry should be utilized wherever possible. On the other hand, there are many important differences, i.e. (i) in a realistic solid, one needs to define the impurity basis, and different definitions can vary widely in terms of locality and other properties, (ii) the number of atoms and basis functions per impurity cell can be very large in a realistic system, and (iii) realistic Hamiltonians contain complicated interactions between all the basis functions, including potentially divergent long-range Coulomb terms. Thus, realizing *ab initio* DMET involves both specifying some, in principle, arbitrary choices (such as the choice of impurity orbitals) as well as carrying out efficient implementations of many standard quantum chemistry routines, such as integrals

and their transformations. The latter is also part of the general infrastructure of *ab initio* periodic quantum chemistry. In this work we rely heavily on the periodic computational infrastructure established in the PYSCF package,^{42–44} which in fact historically grew out of an effort to implement *ab initio* DMET.

The remainder of the paper is organized as follows. In Sec. 2, we first describe the detailed DMET embedding framework for periodic solids, including the definition of the impurity and lattice basis, the construction of local orbitals, bath truncation, efficient integral transformation, and DMET and charge self-consistency. In Sec. 3, we apply the method to some prototype crystals with realistic basis sets and non-trivial cluster sizes with up to ~ 300 embedded cluster orbitals, including a 2D hexagonal boron nitride monolayer, 3D crystalline silicon, and the antiferromagnetic (AFM) II phase of NiO. We finish in Sec. 4 with conclusions and remarks.

Note added: In a recent submission, Pham et al. have also presented related work⁴⁵ that applies *ab initio* DMET to periodic systems.

2 Theory

2.1 DMET Implementation

In this section, we describe the detailed implementation of DMET for *ab initio* calculations in solids, focusing on aspects related to periodic systems that have not been reported in the previous DMET literature. For a general description of the DMET algorithm (and a detailed description of its molecular implementation) we refer readers to Ref. 38.

Lattice and impurity localized orbitals. The infrastructure of *ab initio* mean-field theory uses crystal (Bloch) orbitals and \mathbf{k} -point quantities, while quantum embedding is naturally formulated in terms of local orbitals and real-space quantities. Thus, we first define a translation from the mean-field computational basis to one appropriate for embedding.

To do so, we construct atom-centered orthogonal local orbitals (LO) $\{w_i(\mathbf{r})\}$ that define

the lattice Hilbert space, which can be cleanly partitioned into a product of impurity Hilbert spaces. Here, we will assume that the mean-field computational basis is a set of crystal atomic orbitals (AOs) $\{\phi_\mu^{\mathbf{k}}(\mathbf{r})\}$ (which constitutes a non-orthogonal basis, with an AO index μ and a \mathbf{k} -point index in the first Brillouin zone). It is convenient to first define an intermediate set of local crystal orbitals,

$$w_i^{\mathbf{k}}(\mathbf{r}) = \sum_{\mu} \phi_{\mu}^{\mathbf{k}}(\mathbf{r}) C_{\mu i}^{\mathbf{k}, \text{AO}, \text{LO}}, \quad (1)$$

where the notation $C^{\text{X}, \text{Y}}$ denotes the transformation from basis X to basis Y. The real-space LOs in any cell can then be obtained by a Wannier summation over the local crystal orbitals, for example, the LOs at the lattice origin ($\mathbf{R} = \mathbf{0}$) are given by

$$w_i^{\mathbf{R}=\mathbf{0}}(\mathbf{r}) = \frac{1}{\sqrt{N_{\mathbf{k}}}} \sum_{\mathbf{k}} w_i^{\mathbf{k}}(\mathbf{r}). \quad (2)$$

Expressed in the LOs, the *ab initio* periodic system is isomorphic to a periodic lattice problem, with reciprocal lattice vectors \mathbf{k} . We choose a subset of $\{w_i(\mathbf{r})\}$ to define the impurity. It is natural to choose the impurity to be spanned by LOs in a single unit cell or a supercell, and for definiteness, we choose the cell or supercell at the lattice origin as the impurity.

Choice of local orbitals. The next computational task is to specify the coefficients in Eq. 1 that define the LOs in terms of the crystal AOs. There are two strategies to construct orthogonal local orbitals: a *top-down* strategy [transforming from canonical mean-field molecular orbitals (MOs) to LOs] and a *bottom-up* strategy (transforming from the AO computational basis to LOs). The first strategy finds a unitary transformation of the MOs to optimize a metric (such as $\langle r^2 \rangle - \langle \mathbf{r} \rangle^2$) that measures the spatial locality of the LOs. Examples of such approaches are the Boys,⁴⁶ Pipek-Mezey (PM)⁴⁷ and Edmiston-Ruedenberg (ER)⁴⁸ methods in molecules, and the maximally localized Wannier function (MLWF)^{49,50} and Pipek-Mezey Wannier function (PMWF)⁵¹ methods in solids. The top-down scheme can yield more localized orbitals than bottom-up schemes. However, due to

the need to carry out an optimization, the disadvantages are also apparent: (i) the procedure can be numerically expensive and one can easily get stuck in a local minimum of the cost function, particularly when constructing a large number of local virtual orbitals; (ii) with periodic boundary conditions, entangled bands^{52,53} often exist among the high-energy virtual MOs, and special techniques are required; (iii) a false minimum or discontinuity in \mathbf{k} -space can lead to non-real orbitals after the Wannier summation in Eq. 2, giving a Hamiltonian with complex coefficients in the LO basis, which is incompatible with many impurity solver implementations.

In the bottom-up strategy, one avoids optimization and relies only on linear algebra to construct the LOs. Examples of LOs of this type are the Löwdin and meta-Löwdin orbitals,^{54,55} natural atomic orbitals (NAO)⁵⁶ and intrinsic atomic orbitals (IAO).⁵⁷ Bottom-up methods avoid the difficulties of the top-down strategy: (i) the construction is usually cheap (i.e. suited to producing large numbers of local orbitals); (ii) there is no initial guess dependence or local minimum problem; (iii) the LOs are guaranteed to be real as long as the phases of crystal AOs and other \mathbf{k} -space orbitals in the formalism (e.g. the reference crystal AOs used to construct the IAOs) are smooth in \mathbf{k} -space. Since we aim to carry out calculations beyond a minimal basis, and thus with many virtual orbitals, we have chosen the bottom-up strategy to avoid difficulties in optimization and non-real Hamiltonian coefficients. In particular, we have adapted the molecular IAO routine to crystal MOs with \mathbf{k} -point sampling (see Appendix A) to generate the set of crystal IAOs. The crystal IAOs are *valence* orbitals that exactly span the occupied space of the mean-field calculation. Note that the number of IAOs is the same as the size of the minimal basis only. To obtain a complete set of LOs that span the same space as the original AO basis (thus making a square rotation matrix $C^{\mathbf{k},\text{AO},\text{LO}}$ in Eq. 1) we need to further augment the IAOs with LOs that live purely in the virtual space. Here we choose these additional orbitals to be the projected atomic orbitals (PAO) for non-valence orbitals,⁵⁸ orthogonalized with Löwdin orthogonalization, as originally proposed for local correlation calculations.⁵⁸ The IAOs + PAOs then together

span the complete space of AOs and constitute a complete LO basis. A related scheme has previously been used in the molecular DMET calculations.^{38,59}

DMET bath and truncation. The DMET embedded Hilbert space consists of the impurity LOs and a set of bath orbitals; these together are the embedding orbitals (EOs). We define the bath orbitals in DMET by using the SVD of the mean-field off-diagonal density matrix between the impurity and remaining lattice $\gamma_{ij}^{\mathbf{R}\neq\mathbf{0},\mathbf{0}}$,³⁸

$$\gamma_{ij}^{\mathbf{R}\neq\mathbf{0},\mathbf{0}} = \sum_{\tilde{i}} B_{\tilde{i}}^{\mathbf{R}\neq\mathbf{0}} \Lambda_{\tilde{i}} V_{ij}^{\mathbf{0}\dagger}. \quad (3)$$

where $B^{\mathbf{R}\neq\mathbf{0}}$ gives the coefficients of the bath orbitals and we use “ \sim ” above the orbital indices to denote orbitals in the embedding space. The overall projection from the LO basis to the EO basis then has the following form,

$$C^{\mathbf{R},\text{LO},\text{EO}} = \begin{bmatrix} \mathbb{1} & \mathbf{0} \\ \mathbf{0} & \mathbf{B}^{\mathbf{R}\neq\mathbf{0}} \end{bmatrix}, \quad (4)$$

where the identity block means that the impurity LOs (i.e. the basis defined in Eq. 2) are left unchanged. To transform from the computational crystal AO basis to the embedding orbitals, we multiply two transformations,

$$\begin{aligned} C^{\mathbf{k},\text{LO},\text{EO}} &= \sum_{\mathbf{R}} e^{-i\mathbf{k}\cdot\mathbf{R}} C^{\mathbf{R},\text{LO},\text{EO}}, \\ C^{\mathbf{k},\text{AO},\text{EO}} &= C^{\mathbf{k},\text{AO},\text{LO}} C^{\mathbf{k},\text{LO},\text{EO}}. \end{aligned} \quad (5)$$

Although the DMET bath is formally of the same size as the number of impurity orbitals, the mean-field wavefunction only contains appreciable entanglement between partially occupied LOs on the impurity and corresponding bath orbitals. Very low-lying core and high-energy virtual impurity orbitals thus are not entangled with any bath orbitals. In practice, this manifests as very small singular values $\Lambda_{\tilde{i}}$ and the corresponding singular vectors (bath

orbitals) can vary between different DMET iterations³⁸ leading to difficulties in converging the DMET self-consistency procedure. To eliminate this instability, we use the procedure previously recommended in molecular DMET calculations.³⁸ We first partition the impurity orbitals into core, valence and virtual orbitals, and only carry out the SVD for the impurity valence columns of the off-diagonal density matrix to construct corresponding valence bath orbitals,³⁸ i.e. the index j in Eq. 3 can be constrained to the valence orbitals only. Note that when pseudopotentials are used in the calculation, there is no core subspace, and thus no core bath orbitals appear. With this construction, the number of embedding orbitals is reduced from $2n_{\text{imp}}$ to $n_{\text{imp}} + n_{\text{val}}$, where n_{val} is the number of valence orbitals, which is smaller than the number of impurity orbitals n_{imp} , and we recover smooth DMET convergence.

Constructing the embedding Hamiltonian. Using the EOs defined above, we can construct the DMET embedding Hamiltonian. The embedding Hamiltonian in the DMET *interacting bath* formalism^{37,38} takes the form,

$$\mathcal{H} = \sum_{\tilde{i}\tilde{j}} \tilde{F}_{\tilde{i}\tilde{j}} c_{\tilde{i}}^{\dagger} c_{\tilde{j}} - \mu \sum_{\tilde{i} \in \text{imp}} c_{\tilde{i}}^{\dagger} c_{\tilde{i}} + \frac{1}{2} \sum_{\tilde{i}\tilde{j}\tilde{k}\tilde{l}} \left(\tilde{i}\tilde{j} \middle| \tilde{k}\tilde{l} \right) c_{\tilde{i}}^{\dagger} c_{\tilde{k}}^{\dagger} c_{\tilde{l}} c_{\tilde{j}}. \quad (6)$$

Besides the normal one- and two-particle terms, a chemical potential μ is added to the impurity Hamiltonian so that the number of electrons on the impurity is constrained to be precisely correct. An alternative choice is the DMET *non-interacting bath* formalism.³⁸ In this case, the two-particle interactions are restricted to the impurity orbitals, and interactions on the bath are mimicked by adding the correlation potential to the bath. For further details, we refer to Ref. 38. In this work, we primarily use the interacting bath formalism, and only briefly consider the non-interacting bath formalism for comparison.

To obtain the coefficients of the embedding Hamiltonian, we first transform the Fock matrix from the AOs to the EOs,

$$F^{\mathbf{0},\text{EO}} = \frac{1}{N_{\mathbf{k}}} \sum_{\mathbf{k}} C^{\mathbf{k},\text{AO},\text{EO}\dagger} F^{\mathbf{k},\text{AO}} C^{\mathbf{k},\text{AO},\text{EO}}, \quad (7)$$

where $F^{\mathbf{k},\text{AO}}$ is the Fock matrix in the periodic mean-field calculation. [Note that regardless of the mean-field orbitals used (i.e. Hartree-Fock or DFT), the Fock matrix refers to the Hartree-Fock one-particle Hamiltonian, *not* the Kohn-Sham Hamiltonian]. To eliminate double counting, we subtract the contribution of the embedding electron repulsion integrals (ERIs, see below for their construction) from the transformed Fock matrix $F^{\mathbf{0},\text{EO}}$ in Eq. 7,

$$\tilde{F}_{\tilde{i}\tilde{j}} = F_{\tilde{i}\tilde{j}}^{\mathbf{0},\text{EO}} - \left[\sum_{\tilde{k}\tilde{l}} \left(\tilde{i}\tilde{j} \left| \tilde{k}\tilde{l} \right. \right) \gamma_{\tilde{i}\tilde{k}} - \frac{1}{2} \left(\tilde{i}\tilde{k} \left| \tilde{l}\tilde{j} \right. \right) \gamma_{\tilde{k}\tilde{l}} \right], \quad (8)$$

where γ is the density matrix rotated to the embedding basis.

The construction and integral transformation of the two-particle ERIs of the embedding orbitals can be computationally expensive. A significant reduction in cost is obtained by using density fitting.^{44,60} Density fitting defines the 4-center ERIs in terms of the 3-center ERIs. In the presence of \mathbf{k} symmetry, this takes the form

$$(\mu\mathbf{k}_\mu\nu\mathbf{k}_\nu|\kappa\mathbf{k}_\kappa\lambda\mathbf{k}_\lambda) \approx \sum_L (\mu\mathbf{k}_\mu\nu\mathbf{k}_\nu|L)(L|\kappa\mathbf{k}_\kappa\lambda\mathbf{k}_\lambda), \quad (9)$$

where L is the auxiliary basis and only three \mathbf{k} indices are independent. There are many choices of auxiliary basis and here we will mainly use Gaussian density fitting (GDF), where L is a set of chargeless Gaussian crystal orbitals, with the divergent part of the Coulomb term treated in Fourier space.⁴⁴ [We discuss plane-wave density fitting (FFTDF) in Appendix B]. L has an implicit \mathbf{k} dependence in Eq. 9. This means the 3-center integral $(L|\mu\mathbf{k}_\mu\nu\mathbf{k}_\nu)$ is more precisely written as $(L\mathbf{k}_L|\mu\mathbf{k}_\mu\nu\mathbf{k}_\nu)$, where $\mathbf{k}_L = \mathbf{k}_\mu - \mathbf{k}_\nu + n\mathbf{b}$ due to momentum conservation ($n\mathbf{b}$ is integer multiple of reciprocal lattice vectors). We construct the embedding ERIs starting from the GDF 3-center integrals according to Algorithm 1. In this algorithm, the final contraction step scales as $\mathcal{O}(n_{\mathbf{k}}n_L n_{\text{EO}}^4)$ while the transformation step (\mathbf{k} -AO to \mathbf{k} -EO) scales as $\mathcal{O}(n_{\mathbf{k}}^2 n_L n_{\text{AO}} n_{\text{EO}}^2) + \mathcal{O}(n_{\mathbf{k}}^2 n_L n_{\text{AO}}^2 n_{\text{EO}})$ where we use $n_{\text{AO}}(n_{\text{EO}})$ to denote the number of atomic (embedding) basis functions per cell. Note that n_{EO} is larger than n_{AO} and

Algorithm 1 Pseudocode for the embedding ERI transformation with GDF.

```

1: for all  $\mathbf{k}_L$  do
2:   for  $(\mathbf{k}_\mu, \mathbf{k}_\nu)$  that conserves momentum do
3:     Transform  $(L|\mu\mathbf{k}_\mu\nu\mathbf{k}_\nu)$  to  $(L|\tilde{i}\mathbf{k}_\mu\tilde{j}\mathbf{k}_\nu)$  by  $C^{\mathbf{k},\text{AO},\text{EO}}$  ▷  $\mathbf{k}$ -AO to  $\mathbf{k}$ -EO
4:      $(L|\mathbf{0}\tilde{i}\mathbf{0}\tilde{j}) += \frac{1}{N_{\mathbf{k}}}(L|\tilde{i}\mathbf{k}_\mu\tilde{j}\mathbf{k}_\nu)$  ▷ FT to the reference cell  $\mathbf{R} = \mathbf{0}$ 
5:   end for
6:    $(\tilde{i}\tilde{j}|\tilde{k}\tilde{l}) += \frac{1}{N_{\mathbf{k}}}\sum_L (\mathbf{0}\tilde{i}\mathbf{0}\tilde{j}|L)(L|\mathbf{0}\tilde{k}\mathbf{0}\tilde{l})$  ▷ Contraction for the embedding ERI
7: end for

```

thus the first term is the dominant term. If the number of \mathbf{k} -points is not too large, the contraction is the rate determining step. It is noteworthy that the scaling with respect to \mathbf{k} is only linear (contraction) and quadratic (transformation). As an example, the embedding ERIs of a $3 \times 3 \times 1$ cluster of boron nitride (GTH-DZVP basis and a $6 \times 6 \times 1$ mean-field lattice corresponding to transforming 936 crystal AOs to 306 embedding orbitals) can be constructed in about 200s using 28 cores. The largest objects during the calculation are the final set of ERIs $(\tilde{i}\tilde{j}|\tilde{k}\tilde{l})$ and the AO density fitting integral $(L|\mu\mathbf{k}_\mu\nu\mathbf{k}_\nu)$. The latter is stored on disk and loaded into memory blockwise to further reduce the required memory. Finally, we note that if the impurity solver supports density fitting without requiring explicit ERIs, the contraction step in Algorithm 1 can be omitted.

DMET and charge self-consistency. A key component in the DMET description of phases and order parameters is the imposition of self-consistency between the “high-level” (HL) embedded wavefunction and the “low-level” (LL) mean-field description. We matched the correlated one-particle density matrix γ from the impurity solver and the mean-field one-particle density matrix by minimizing their Frobenius norm difference with respect to the correlation potential u ,

$$\min_u \sum_{ij \in \text{EO}} [\gamma_{ij}^{\text{LL}}(u) - \gamma_{ij}^{\text{HL}}]^2, \quad (10)$$

where the indices i, j loop over all embedding orbitals and the high-level density matrix γ_{ij}^{HL} is kept fixed during the correlation potential fitting. Other choices of cost function are also possible, e.g. only matching the impurity^{37,38} or diagonal part¹⁹ of the density matrix.

However, we only consider full matching in this work. The correlation potential is a local term (i.e. independent of the impurity cell \mathbf{k}). In the current work, the correlation potential is chosen to be a spin-dependent potential where the number of independent elements per spin-component is $n_{\text{LO}}(n_{\text{LO}} + 1)/2$. With large basis sets, the number of parameters in u can be very large. To reduce the degrees of freedom in the numerical optimization, we can add u only to a subset of orbitals, e.g. the valence orbitals. With a small set of parameters, the optimization problem can be easily solved, e.g. by a conjugate gradient algorithm. It should be noted that the minimization of the cost function is not a convex problem, thus in principle there can be multiple local minima; for example in an AFM system, there may be multiple solutions corresponding to different spin polarization patterns. However, we have not observed multiple local minima in this work, since the BN and Si systems do not break spin symmetry, and in NiO, we always start with a particular AFM order in the initial guess of u .

In an *ab initio* DMET calculation, an additional layer of self-consistency appears associated with the non-linear *ab initio* lattice mean-field calculation [this is sometimes referred to as *charge self-consistency* (CSC) in DMFT calculations^{61–64}]. In our implementation, the AO-based Fock matrix $F^{\mathbf{k},\text{AO}}$ is updated at the beginning of each DMET cycle, using the improved DMET mean-field density matrix from the previous iteration, which reflects the response of the mean-field density (matrix) to the DMET local correction. We always perform CSC in our calculations unless otherwise specified.

We finally note that the LOs, in principle, can be redefined based on the new mean-field MOs at each DMET iteration. However, we do not consider such an update in the current work. Instead, we only determine the LOs at the beginning of the calculation and keep the LOs fixed in the following DMET self-consistency loops. This choice introduces a small dependence on the initial orbitals (e.g. using HF- or DFT-MOs to define the LOs). However, it is usually reasonable to assume that the LOs do not change significantly during the embedding self-consistency.

We illustrate the periodic *ab initio* DMET algorithm, with both DMET correlation potential and charge self-consistency, in Fig. 1.

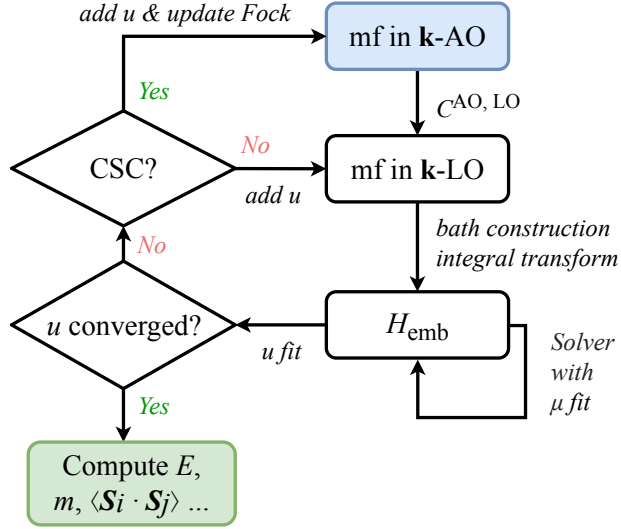


Figure 1: The DMET self-consistency procedure, where “mf” is used to denote the relevant mean-field physical quantities, e.g. the Fock matrix F , density matrix γ ; μ and u are used to denote the chemical potential and correlation potential respectively. “CSC” denotes charge self-consistency and is an optional step in the algorithm. The flowchart starts at the blue block and ends at the green block when self-consistency is reached.

2.2 Computational Details

We consider three prototypical solids: a 2D hexagonal boron nitride monolayer (h-BN), crystalline silicon (Si) and nickel monoxide (NiO). The lattice parameters were taken from experiment: $a = 2.50\text{\AA}$ for the BN monolayer⁶⁵ (with 20.0\AA vacuum to eliminate fictitious interactions between mirrors); $a = 5.43053\text{\AA}$ for Si,⁶⁶ and $a = 4.17\text{\AA}$ for NiO.⁶⁷ To target the AFM-II state, the minimal unit cell of NiO was chosen as the rhombohedral cell that contains two formula units of NiO. We used 28 Intel E5-2680@2.40GHz cores in all the calculations. We summarize the computational parameters for DMET below.

Mean-field calculations. All mean-field calculations were performed using the PYSCF package⁴² with Hartree-Fock or DFT [Perdew-Burke-Ernzerhof (PBE) functional⁶⁸]. GTH pseudopotentials^{69,70} were used to replace the sharp core electron density, with corresponding

GTH-DZVP ($2s2p3s3p3d$ AOs for B and N, and $3s3p3d4s4p$ AOs for Si) and GTH-DZVP-MOLOPT-SR ($3s3p3d4s4p4d4f5s$ AOs for Ni, and $2s2p3s3p3d$ AOs for O) basis sets⁷¹ used to represent the valence electrons. Gaussian density fitting was used to compute the two-electron integrals.⁴⁴ We used an even-tempered Gaussian basis⁷² as the density fitting auxiliary basis, i.e. $L_{nl}(r) \propto r^l \exp(\alpha\beta^n r^2)$, where we used the exponential factor $\beta = 2.3$ for NiO and $\beta = 2.0$ for all other systems. The number of fitting functions was chosen to ensure high accuracy, and thus the size of the auxiliary basis is about 10 times as large as the number of AOs. The GTH-SZV (h-BN and Si) and GTH-SZV-MOLOPT-SR (NiO) basis functions were used as the reference free-atom AOs to construct the IAOs. In the mean-field calculations used to derive the embedding Hamiltonian and in the DMET self-consistency, we sampled the Brillouin zone with a Γ centered mesh chosen so as to be able to fit unit multiples of the DMET impurity supercell. These included a $6 \times 6 \times 1$ mesh for BN, and a $4 \times 4 \times 4$ mesh for Si and NiO. Larger meshes were used in independent estimates of the mean-field TDL for BN (up to $12 \times 12 \times 1$) and Si (up to $8 \times 8 \times 8$). All mean-field calculations were converged to an accuracy of better than 10^{-10} a.u. per unit cell. In the case of Hartree-Fock energies, all energies included the leading-order exchange finite-size correction (probe-charge Ewald,^{73,74} `exxdiv=ewald` in PYSCF). Note that the above correction applies to all DMET energies as these use the Hartree-Fock expression for the mean-field energy even when density functional orbitals are used.

Impurity solver. We used coupled cluster singles and doubles (CCSD)⁷⁵ as an impurity solver, as implemented in PYSCF,⁴² which is able to treat a large number of orbitals efficiently. In NiO where DMET self-consistency produced symmetry breaking, we used unrestricted CCSD (UCCSD). The CC density matrices were obtained from the CC Λ equations.⁷⁶ The CC energies were converged to 10^{-8} a.u..

DMET self-consistency. For BN and NiO, the correlation potential u was added to only the valence orbitals and for Si, u was added to all impurity orbitals as this gave smoother DMET convergence. We carried out CSC calculations for all three systems, and included

additional non-CSC results of NiO for comparison. The convergence criterion on the DMET self-consistency was chosen such that the maximal change of an element in u was less than 5×10^{-5} a.u., which corresponded roughly to an energy accuracy of better than 1×10^{-5} a.u..

3 Results and Discussion

3.1 2D Boron Nitride

We first study the behavior of DMET on a 2D boron nitride monolayer. In a GTH-DZVP basis, BN has a unit cell of 2 atoms, with $2s2p$ AOs on each atom giving 8 valence orbitals per cell, and $3s3p3d$ AOs on each atom providing 18 higher-energy virtual orbitals per cell. We illustrate the valence IAOs of boron in BN in Fig. 2(a). As expected, the IAOs of boron are

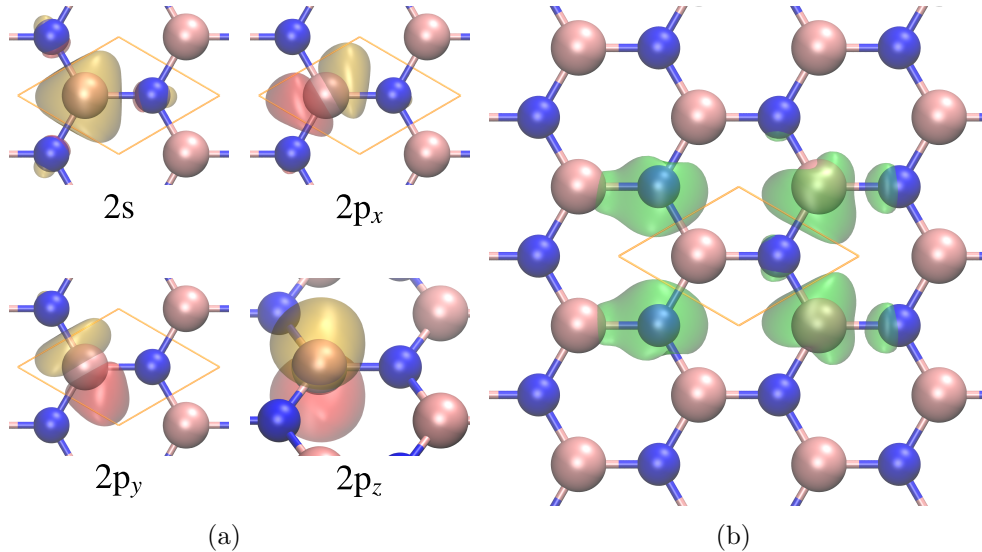


Figure 2: Impurity orbitals and bath density of BN used in the DMET calculations. The boron and nitrogen atoms are colored pink and blue respectively. (i) Impurity valence orbitals associated with one boron atom (IAOs from boron). (ii) Bath orbital density coupled to the first reference cell.

quite local, retaining their original AO character but with some slight polarization to reflect the mean-field solution in the crystal environment. The bath orbital density is plotted in Fig.

2(b) (we only show the total density summed over the bath orbitals here, since the embedded problem only depends on the linear span of the bath). It is clear that the bath orbitals are localized around the impurity cluster and give an effective representation of the remainder of the boron nitride crystal. In particular, the bath orbitals serve to terminate the dangling bonds on the impurity boundary, thus turning the embedding problem into a closed-shell one at the mean-field level. The impurity valence orbitals and bath orbitals pictured here, together with the impurity virtual orbitals (not shown), constitute the embedding orbitals.

We computed total energies (per cell) from DMET for different cluster sizes, 1×1 , 2×2 and 3×3 . We compare these total energies to those from \mathbf{k} -sampled periodic CCSD (\mathbf{k} -CCSD) extrapolated to the TDL (see Fig. 3) which has recently been demonstrated to be a high accuracy method in a variety of different materials.^{43,77,78} Note that, accounting fully for the \mathbf{k} -point symmetry, \mathbf{k} -CCSD has a computational scaling of $n_{\text{AO}}^6 n_{\mathbf{k}}^4$. The reference TDL \mathbf{k} -CCSD energy is the sum of the extrapolated HF energy using a large \mathbf{k} -mesh (up to $12 \times 12 \times 1$, extrapolating with the form $n_{\mathbf{k}}^{-1}$ after using the Ewald exchange divergence correction^{73,79}) and the extrapolated \mathbf{k} -CCSD correlation energy using a smaller \mathbf{k} -mesh (up to $6 \times 6 \times 1$, extrapolating with the form $n_{\mathbf{k}}^{-1}$). Compared to the TDL reference energy, even using the smallest (1×1) cluster, DMET gives an accurate total energy that captures about 95% of the correlation energy. Extrapolating over the DMET cluster size (using the surface to volume form $N_c^{-1/2}$, where N_c is the cluster size) further improves the accuracy by about 1-2% in the correlation energy. The one-shot DMET result (i.e. without DMET self-consistency) is less accurate than the self-consistent one by ~ 8 mHartree (3% of the correlation energy), demonstrating the contribution of self-consistent matching between the high-level calculation and the low-level mean-field calculation. We note that self-consistency is generally not very important in non-magnetic weakly-correlated systems, as there are no symmetry broken phases to be generated by DMET, and only provides a modest quantitative correction to the observables.

Compared to small $N \times N \times 1$ \mathbf{k} -mesh CCSD energies, the DMET total energies are

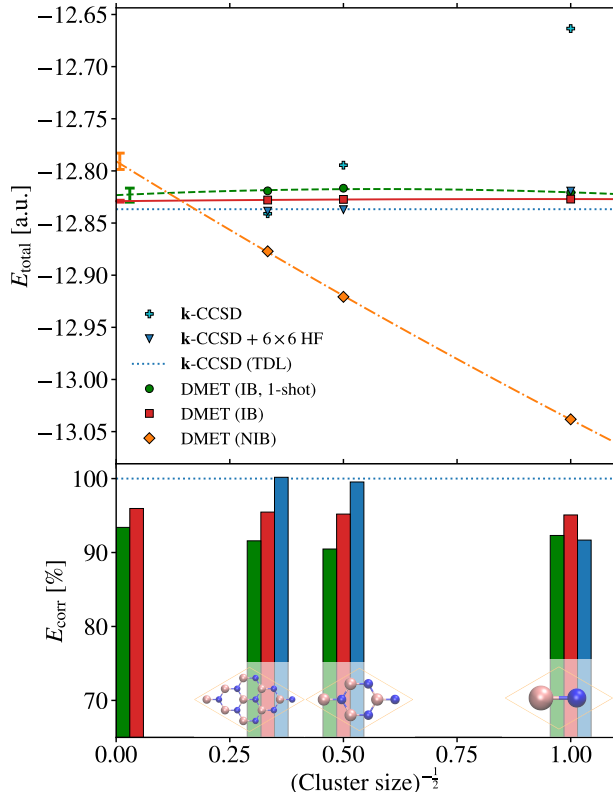


Figure 3: Upper panel: Total energy from DMET compared with \mathbf{k} -sampled CCSD. In the case of DMET with the interacting bath (IB), both one-shot and self-consistent energies are reported. DMET with non-interacting bath (NIB) is also shown for comparison. The extrapolated values of DMET is from an average of linear regression and quadratic fitting. The error bar is the difference between the linear and quadratic fitted values. We plot the energy of \mathbf{k} -CCSD with small \mathbf{k} -mesh (one curve with HF energy at corresponding small \mathbf{k} -mesh and the other with HF energy at 6×6 \mathbf{k} -mesh) and the extrapolated TDL results as reference. Lower panel: Correlation energy ratio with respect to the extrapolated CCSD correlation energy.

more accurate for the 1×1 and 2×2 cluster sizes, but less accurate for the 3×3 case. The finite size error in the total energy, arising from the finite \mathbf{k} -mesh or DMET cluster size, can be separated into two sources, (i) the finite size error in the mean-field energy and (ii) the finite size error in the many-body correlation energy. For embedding methods like DMET, the error from the first source is (largely) eliminated. Thus, as shown in Fig. 3, the DMET total energy is good even for a small cluster size. In the CCSD calculation, however, the error from (i) is large for small clusters, and therefore, a potentially better recipe for the total energy is to sum the HF energy from a larger cluster (or even extrapolated to the TDL)

and the correlation energy from the small cluster calculation. In the upper panel, we show the \mathbf{k} -CCSD correlation energy added to the 6×6 HF energy (corresponding to the size of the DMET lattice), as well as to the extrapolated TDL HF energy. Together with the data in the lower panel of Fig. 3, we see that the correlation energy E_{corr} of CCSD, which relies on the above error cancellation, is already very accurate for the 2×2 cluster and is better than that of DMET for this cluster size. It is then worth analyzing the source of errors in the small cluster DMET correlation energy. One source is the lack of embedding of the non-valence virtual orbitals, which are localized to the reference cell with the periodicity of the large DMET mean-field lattice, not the periodicity of the impurity (as in the \mathbf{k} -CCSD calculation). The advantages of DMET in the current implementation thus manifest when the predominant correlation is within the valence space itself (which is fully embedded) as is typical of strong correlations, rather than primarily involving excitations to non-embedded, non-valence, virtual orbitals as in this system. One way to diminish the boundary effect on the DMET non-valence virtuals is to evaluate the energy from the central part of the supercell, for which the surrounding atoms effectively provide a bath for the virtuals. We find then that the energy evaluated using the central cell of the embedded cluster covers 103.8% of the correlation energy (using the preceding 3×3 cluster calculation) or 100.1% (if no chemical potential fitting is used), which is better than that obtained by direct energy evaluation using the entire embedded cluster. It may be possible to further reduce this boundary error using the dynamical cluster approximation formulation of DMET (DCA-DMET)²² or bootstrap embedding.⁸⁰⁻⁸²

We finally consider DMET results obtained using the non-interacting bath (NIB), as also shown in Fig. 3. We see that although the extrapolation is quite systematic, the accuracy is worse than that of the interacting bath for all three cluster sizes. This result is generally found in chemical systems with long-range Coulomb interactions, as the interacting bath carries some information about the inter-cluster interactions. However, the NIB formalism has the potential computational advantage that the construction of the NIB embedded Hamiltonian

is cheaper than the IB one, since only the impurity part of the two-particle Hamiltonian is needed. In addition, the correlation potential can be used to mimic the effect of the long-range Coulomb contributions to the Fock matrix. This makes the NIB scheme an interesting possibility in large systems.

3.2 Bulk Silicon

We next test the ability of DMET to describe the structural properties of bulk Si. We performed a series of calculations on different primitive cell volumes and fitted the relative total energy E as a function of the volume V using the Birch-Murnaghan (B-M) equation of state (EOS),^{83,84} from which the equilibrium volume and bulk modulus can then be determined. To obtain accurate results for the TDL, we considered three clusters of different shapes: a $1 \times 1 \times 1$ primitive cell (2 Si atoms), a conventional diamond cubic cell (8 Si atoms) and a $2 \times 2 \times 2$ supercell (16 Si atoms). We performed the extrapolation with respect to cluster volume V_c using

$$E(V_c) = E(\infty) + a_0 V_c^{-1/3} + \dots \tag{11}$$

The total energy includes the correction from HF at the TDL. The equilibrium volumes and bulk moduli are collected in Table 1.

Table 1: Equilibrium volume of the primitive cell V_0 and bulk modulus B_0 of silicon from different approaches. The extrapolated values are from the linear fit of $1 \times 1 \times 1$ and $2 \times 2 \times 2$ results. The CCSD results are taken from Ref. 43, which uses the larger GTH-TZVP basis. The experimental V_0 is from Ref. 66 and B_0 is from Ref. 85 with a zero-point correction.

Methods		V_0 [\AA^3]	B_0 [GPa]
HF	extrap.	40.30	107
DMET	$1 \times 1 \times 1$	42.83	87.9
	cubic cell	41.90	88.5
	$2 \times 2 \times 2$	41.26	91.1
	extrap.	39.69	99.0
CCSD	$3 \times 3 \times 3$	39.21	103
Expt.		40.04	101

From the table, we see that the equilibrium volume of DMET using the $1 \times 1 \times 1$ cluster

deviates from the experimental value by 7%. The error from the smallest impurity cluster is thus larger for Si than for BN. This is because Si has a much smaller band gap and thus less local correlation involving the non-valence space. However, the results improve rapidly when increasing the size of cluster. To illustrate this, we show the EOS curves for different cluster sizes in Fig. 4. It is clear that the $1 \times 1 \times 1$ curve is shifted to larger volume

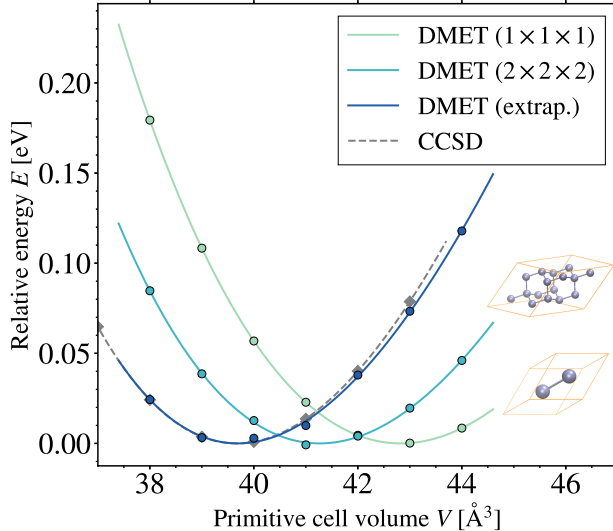


Figure 4: Equation of state curves of Si from DMET and CCSD. For DMET, we omit the cubic cell curve for clarity. CCSD data is taken from Ref. 43.

compared to experiment or CCSD. Increasing the cluster size systematically shifts the curve back towards experiment and the \mathbf{k} -CCSD benchmark, resulting in a very small relative error (w.r.t. experiment) of 0.9% for V_0 for the extrapolated curve. The extrapolated bulk modulus B_0 also agrees well with the experimental and \mathbf{k} -CCSD benchmark values. Overall, the accuracy achieved by extrapolated DMET appears comparable to that of the \mathbf{k} -CCSD benchmark in a full $3 \times 3 \times 3$ periodic calculation, although we note that a different basis was used.

3.3 Nickel monoxide

We now demonstrate the ability of DMET to treat a more strongly correlated problem by considering a typical transition metal compound, NiO. Below the Néel temperature, NiO

displays an antiferromagnetic (AFM) phase with a staggered magnetization along the [111] direction (the so-called AFM-II phase). Although DFT (with PBE) and HF do predict spin-polarization, it is known that DFT often underpolarizes while HF often overpolarizes antiferromagnetic states. To avoid such biases in the DMET calculation, we embed the DMET calculation in an initial *unpolarized* mean-field state. We constructed the unpolarized mean-field state by using the orbitals obtained from the spin-averaged Fock matrix of an unrestricted Hartree-Fock or DFT calculation. We use the spin-averaged Fock matrix for convenience because without finite-temperature smearing, the restricted calculations either have difficulty converging due to the metallic nature (DFT) or exhibit an unphysical symmetry breaking of the density between the symmetry-equivalent nickel atoms (HF). The spin-averaged Fock matrix is similar to the restricted one with smearing but exactly preserves the symmetry between the two nickel atoms. We denote DMET calculations based on the spin-averaged mean-field orbitals by $\text{DMET@}\Phi_{\text{RHF}}^*$ ($\text{DMET@}\Phi_{\text{RPBE}}^*$), where “*” means the restricted orbitals are actually from the spin-averaged unrestricted Fock matrix rather than a real restricted one.

The spectrum of such a spin-averaged Fock matrix is gapless. After adding an initial DMET correlation potential, e.g. taken from the local part of the UHF polarized potential, the system becomes gapped and S^2 symmetry is broken. Without CSC, the final DMET mean-field gap is ~ 3 eV and with CSC, the DMET mean-field gap is ~ 10 eV, closer to the Hartree-Fock mean-field gap (~ 12 eV). (Note that the experimental band gap of AFM NiO is ~ 4.3 eV⁸⁶). It should be emphasized that although the band gap from the DMET lattice mean-field reflects the insulating nature of the system, its value does not correspond to the true fundamental gap of the system. Even if the density from the impurity solver were exact and the matching between density matrices were perfect, the mean-field gap is not exact due to the derivative discontinuity contribution,⁸⁷ similar to the Kohn-Sham gap obtained from an optimized effective potential (OEP) calculation.⁸⁸

The ground state charges and local magnetic moments of NiO from DMET starting

from different initial mean-fields (spin-averaged HF and PBE) are summarized in Table 2. Assignment of local observables to different atoms (population analysis) was performed using the IAOs + PAOs and the density matrix from the CC impurity solver. We also include

Table 2: Local charge (in e) and magnetic moment (in μ_B) of NiO from different methods. The values on Ni (O) are averaged from the two Ni (O) sites in the primitive cell. We include the DMET results from different initial orbitals (Φ_{RHF}^* and Φ_{RPBE}^*), with / without charge self-consistency (CSC). The experimental data is taken from Refs. 67,89,90.

Methods	ρ_{Ni}	m_{Ni}	m_{O}
HF	1.42	1.86	0.000
PBE	1.02	1.42	0.000
DMET@ Φ_{RHF}^* w/o CSC	1.32	1.77	0.018
DMET@ Φ_{RPBE}^* w/o CSC	1.27	1.74	0.017
DMET@ Φ_{RHF}^* w/ CSC	1.37	1.81	0.001
DMET@ Φ_{RPBE}^* w/ CSC	1.35	1.78	0.000
Expt.		1.70-1.90	

unrestricted HF, PBE results for comparison.

First, we observe clear charge transfer from Ni to O in all methods. Among them, HF gives the largest ionic character while PBE smears out the charge and predicts the smallest charge transfer. The DMET results from different starting orbitals and CSC conditions are between these two limits and are relatively close to each other. The DMET results with CSC (starting from HF and PBE) are particularly close to each other as the inter-cluster part of density matrix is updated using information from the high-level embedded calculation. In fact, in the case of CSC, the only effect of the initial choice of orbitals in DMET on the final result comes from the different definition of the local orbitals.

Compared to the experimental estimate of the magnetic moment, unrestricted Hartree-Fock gives a Ni magnetic moment at the higher-end of the experimental range, while PBE severely underestimates the magnetic moment. DMET yields results independent of the starting orbitals with a moment that agrees well with experiment. To illustrate the AFM distribution in NiO, we plot the spin density distribution in the (001) plane of NiO in Fig. 5. In the figure, the α - and β - spin planes alternately appear along the diagonal direction,

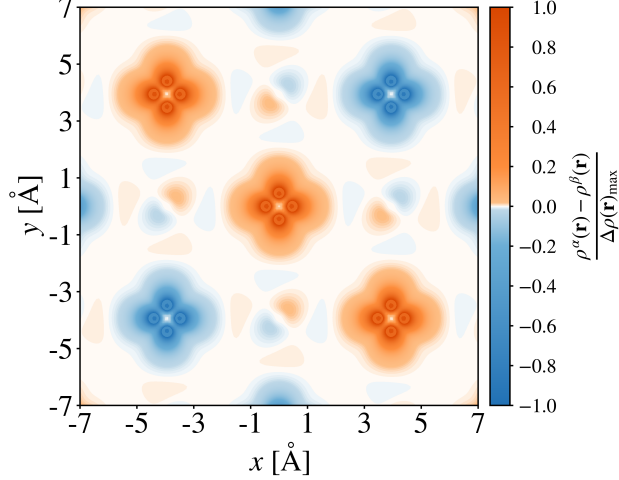


Figure 5: Spin density $\rho_\alpha - \rho_\beta$ on the (001) plane of NiO from DMET@ Φ_{RHF}^* with charge self-consistency.

showing a clear AFM pattern. In particular, the spin density on Ni is in the shape of the $d_{x^2-y^2}$ orbital, indicating that its occupation is asymmetric with respect to the α and β electrons. In fact, the t_{2g} orbitals are almost fully occupied ($\sim 5.97 e$ in our population analysis), and the e_g orbitals ($d_{x^2-y^2}$ and d_{z^2}) are occupied only in one spin sector ($\sim 1.99 e$), and roughly empty in the other ($\sim 0.19 e$). The local magnetic moment on Ni therefore mainly comes from the contribution of the e_g electron density, as expected from crystal field theory. The density on oxygen is in the shape of a p orbital and is polarized according to its orientation relative to Ni. The average polarization on oxygen should be close to zero due to symmetry. As shown in Table 2, the magnetic moments on oxygen from DMET (especially with CSC) are indeed close to zero.

We now take a closer look at the spin-spin correlation in NiO. To this end, we evaluate the spin-spin correlation function between the two nickels in the unit cell,

$$\sum_{i \in \text{Ni}_1, j \in \text{Ni}_2} \langle \mathbf{S}_i \cdot \mathbf{S}_j \rangle = \sum_{i \in \text{Ni}_1, j \in \text{Ni}_2} \sum_{a=x,y,z} \langle S_i^a S_j^a \rangle, \quad (12)$$

where i and j are the indices of LOs located on the first and second Ni respectively. In the DMET@ Φ_{RHF}^* calculation with charge self-consistency, the expectation value is -0.8147 ,

where the minus sign arises from the AFM correlation between the spins of two nickels. This value, however, is very close to the product $\langle S^z \rangle \langle S^z \rangle = -0.8149$. In addition, the spin non-collinear contributions ($\langle S^x S^x \rangle$ and $\langle S^y S^y \rangle$) are almost zero (note that the calculation spontaneously chooses a z magnetization axis due to the initial unrestricted Hartree-Fock reference or form of the correlation potential). All these features suggest that the ground-state of the AFM spin lattice in NiO is close to that of a classical Ising model, rather than a quantum one. Our results are consistent with experimental measurements on the critical behavior of the magnetic phase transition in NiO,⁹¹⁻⁹³ where the critical exponents are found to be very close to those of the 3D Ising model.

In the above results, we found that the DMET order parameters are insensitive to the initial mean-field orbitals, due to the DMET self-consistency. As discussed in section 2.1, this self-consistency contains two different contributions: self-consistency of the DMET correlation potential (expressed along the cluster blocks of the mean-field lattice Hamiltonian) and charge self-consistency of the mean-field Fock operator (for the off-diagonal blocks of the mean-field lattice Hamiltonian). To show the robustness of the self-consistency with respect to the correlation potential guess and the relative magnitude of these two contributions, we show the convergence of the local magnetic moment of Ni with respect to the number of iterations in Fig. 6 (for initial restricted orbitals from a spin-averaged Fock matrix Φ_{RHF}^*) with two different initial guesses for the correlation potential: the strongly polarized UHF potential, and a weakly polarized potential equal to the UHF potential scaled by a factor 0.1, both with and without charge self-consistency. From the figure, we see that starting from different initial guesses for the correlation potential, the magnetic moments from non-self-consistent (i.e. one-shot) DMET (the 0th iteration in Fig. 6) can be very different. However, after only 1 step, the magnetic moments are significantly improved. Eventually, the magnetic moments from the two guesses converge to a very similar value, showing that the DMET self-consistency effectively removes the initial correlation potential guess dependence. The picture with and without charge self-consistency is very similar, showing that the DMET

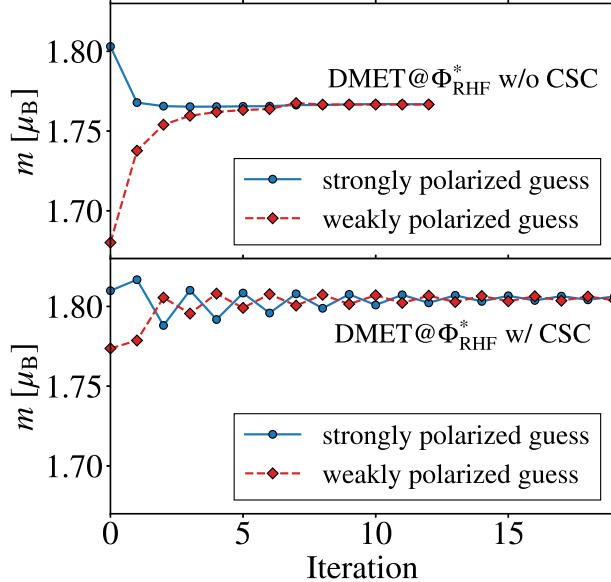


Figure 6: The convergence of the magnetic moment on Ni from different initial correlation potentials. Upper panel: DMET@ Φ_{RHF}^* without CSC using different initial guesses: UHF potential (strongly polarized) or UHF potential scaled by 0.1 (weakly polarized). Lower panel: The same as the upper panel but with CSC.

correlation potential is the main factor controlling the local order parameter. Note that in Fig. 6, the LOs are the same (based on Hartree-Fock) for all calculations and hence there is no initial LO dependence. Finally, as a rough indicator of cost, each DMET iteration takes about 1 hour (the computational setup is described in Sec. 2.2).

4 Conclusions

In this paper, we described an *ab initio* quantum embedding scheme for density matrix embedding calculations in solids, focusing on the practical implementation choices needed for an efficient computational scheme. Our tests on the BN, Si, and NiO systems, that span a range of electronic structure, demonstrate that our implementation can handle both realistic unit cells and basis sets. The strengths of DMET are most visible in the simulations of NiO, where the wide spread in magnetic behavior generated by different mean-field approximations is almost entirely removed in the subsequent DMET calculation. In more weakly correlated

systems, more work is needed to improve the quantitative accuracy of DMET arising from the treatment of excitations to non-valence orbitals, which are not fully embedded in our scheme. Overall, however, our results lead us to be optimistic that this computational framework provides a means to realize *ab initio* calculations on interesting correlated solids using density matrix embedding theory. Much of the computational framework can be reused also to realize *ab initio* dynamical mean-field theory (DMFT) in solids, and elsewhere, we report the results of such a scheme.⁹⁴

Acknowledgement

We thank James McClain for providing CCSD data on the equation of state of Si, Lin Lin and Yang Gao for helpful discussions and Mario Motta for helpful comments on the manuscript. This work is partially supported by US Department of Energy via award no. DE-SC19390. Additional support was provided by the Simons Foundation via an Investigatorship and through the Simons Collaboration on the Many-Electron Problem.

A k-adapted IAO and PAO

The key ingredients for IAO construction⁵⁷ are the occupied MOs $\{|\psi_m\rangle\}$ and two sets of bases, B_1 and B_2 . Concretely, B_1 is the normal AO basis used in the mean-field calculation (labeled by μ, ν, \dots) and B_2 is the reference minimal basis set (labeled by ρ, σ, \dots). B_1 usually contains the space of B_2 and the extra part reflects the polarization. The goal of IAO construction is to obtain a set of AO-like orbitals that contains the occupied space but has the size of the small basis set B_2 . To achieve this, we first define the *depolarized* MOs $\{|\psi_{\bar{m}}\rangle\}$ by projecting the MOs to B_2 , then back to B_1 ,

$$|\psi_{\bar{m}}\rangle = \text{orth}(P^{B_1} P^{B_2} |\psi_m\rangle), \quad (13)$$

where P is the resolution of identity (or projector) of AOs, e.g.

$$P_{\mu\nu}^{B_1} = \sum_{\mu\nu} |\phi_\mu\rangle S_{\mu\nu}^{B_1} \langle\phi_\nu|. \quad (14)$$

Using the depolarized MO projector $\bar{O} \equiv \sum_{\bar{m}} |\psi_{\bar{m}}\rangle\langle\psi_{\bar{m}}|$, we can split the B_2 set into occupied ($\bar{O}|\phi_\rho\rangle$) and virtual spaces $(1 - \bar{O})|\phi_\rho\rangle$. The IAOs $\{|w_i\rangle\}$ are obtained by further projecting these two subspace bases onto their polarized counterparts ($O \equiv \sum_m |\psi_m\rangle\langle\psi_m|$ and $1 - O$) and applying Löwdin orthogonalization,

$$|w_i\rangle = \text{orth}\{[O\bar{O} + (1 - O)(1 - \bar{O})]|\phi_\rho\rangle\}. \quad (15)$$

In periodic systems, the quantities in the above equations should be understood to carry \mathbf{k} labels, e.g. $|\phi_\mu\rangle \rightarrow |\phi_\mu^{\mathbf{k}}\rangle$ is a crystal AO, and $S^{B_1} \rightarrow S^{\mathbf{k},B_1}$ is the corresponding overlap matrix. These quantities are already evaluated in the mean-field calculations. The only thing we need additionally is the overlap matrix between basis B_1 and B_2 , which can be evaluated directly,

$$S_{\mu\rho}^{\mathbf{k},B_1,B_2} = \int d\mathbf{r} \sum_{\mathbf{T}} e^{i\mathbf{k}\cdot\mathbf{T}} \phi_\mu^*(\mathbf{r}) \phi_\rho(\mathbf{r} - \mathbf{T}), \quad (16)$$

where the summation is over the periodic images \mathbf{T} . After the IAOs are constructed, the \mathbf{k} -adapted PAOs are obtained by projecting out the IAO components from the AOs at each \mathbf{k} -point.

B Embedding ERI construction with FFTDF

The embedding ERIs can also be constructed from FFTDF, which uses the fast Fourier transform to represent the Coulomb kernel and to expand the AO pairs. In such a case, L

in Eq. 9 is a set of planewaves $\{\mathbf{G}\}$,⁴³

$$(\mu\mathbf{k}_\mu\nu\mathbf{k}_\nu|\kappa\mathbf{k}_\kappa\lambda\mathbf{k}_\lambda) \approx \Omega^2 \sum_{\mathbf{G}} (\mu\mathbf{k}_\mu\nu\mathbf{k}_\nu|\mathbf{G}) \frac{4\pi}{\Omega|\mathbf{q}+\mathbf{G}|^2} (-\mathbf{G}|\kappa\mathbf{k}_\kappa\lambda\mathbf{k}_\lambda), \quad (17)$$

where Ω is the volume of the unit cell, $\mathbf{q} \equiv \mathbf{k}_\mu - \mathbf{k}_\nu$ and only three \mathbf{k} s are independent. Similarly to the algorithm for GDF, the AO-to-EO transformation can be performed on the 3-index quantities. The procedure is described in Algorithm 2.

Algorithm 2 Pseudocode for embedding ERI transformation with FFTDF.

```

1: for all  $\mathbf{q}$  do
2:   for  $(\mathbf{k}_\mu, \mathbf{k}_\nu)$  that conserves momentum do
3:     Transform  $(\mathbf{r}|\mu\mathbf{k}_\mu\nu\mathbf{k}_\nu)$  to  $(\mathbf{r}|\tilde{i}\mathbf{k}_\mu\tilde{j}\mathbf{k}_\nu)$  by  $C^{\mathbf{k},\text{AO},\text{EO}}$  ▷ k-AO to k-EO
4:      $(\mathbf{r}|\mathbf{0}\tilde{i}\mathbf{0}\tilde{j}) += \frac{1}{N_{\mathbf{k}}} (\mathbf{r}|\tilde{i}\mathbf{k}_\mu\tilde{j}\mathbf{k}_\nu)$  ▷ FT to the reference cell  $\mathbf{R} = \mathbf{0}$ 
5:   end for
6:   Calculate  $(\mathbf{G}|\mathbf{0}\tilde{i}\mathbf{0}\tilde{j})$  using FFT
7:    $(\mathbf{G}|\mathbf{0}\tilde{i}\mathbf{0}\tilde{j}) *= \frac{4\pi}{\Omega|\mathbf{q}+\mathbf{G}|^2}$ 
8:   Calculate  $(\mathbf{r}|\mathbf{0}\tilde{i}\mathbf{0}\tilde{j})$  using inverse FFT
9:   for  $(\mathbf{k}_\kappa, \mathbf{k}_\lambda)$  that conserves momentum do
10:    Transform  $(\mathbf{r}|\kappa\mathbf{k}_\kappa\lambda\mathbf{k}_\lambda)$  to  $(\mathbf{r}|\tilde{k}\mathbf{k}_\kappa\tilde{l}\mathbf{k}_\lambda)$  by  $C^{\mathbf{k},\text{AO},\text{EO}}$  ▷ k-AO to k-EO
11:     $(\mathbf{r}|\mathbf{0}\tilde{k}\mathbf{0}\tilde{l}) += \frac{1}{N_{\mathbf{k}}} (\mathbf{r}|\tilde{k}\mathbf{k}_\kappa\tilde{l}\mathbf{k}_\lambda)$  ▷ FT to the reference cell  $\mathbf{R} = \mathbf{0}$ 
12:   end for
13:    $(\tilde{i}\tilde{j}|\tilde{k}\tilde{l}) += \frac{1}{N_{\mathbf{k}}} \sum_{\mathbf{r}} (\mathbf{0}\tilde{i}\mathbf{0}\tilde{j}|\mathbf{r}) (\mathbf{r}|\mathbf{0}\tilde{k}\mathbf{0}\tilde{l})$  ▷ Contraction for the embedding ERI
14: end for

```

References

- (1) Imada, M.; Fujimori, A.; Tokura, Y. Metal-insulator Transitions. *Rev. Mod. Phys.* **1998**, *70*, 1039–1263.
- (2) Dagotto, E. Correlated Electrons in High-Temperature Superconductors. *Rev. Mod. Phys.* **1994**, *66*, 763–840.
- (3) Sachdev, S. Colloquium: Order and Quantum Phase Transitions in the Cuprate Superconductors. *Rev. Mod. Phys.* **2003**, *75*, 913.

- (4) Lee, P. A.; Nagaosa, N.; Wen, X.-G. Doping a Mott Insulator: Physics of High-Temperature Superconductivity. *Rev. Mod. Phys.* **2006**, *78*, 17.
- (5) Zgid, D.; Chan, G. K.-L. Dynamical Mean-field Theory from a Quantum Chemical Perspective. *J. Chem. Phys.* **2011**, *134*, 094115.
- (6) Sun, Q.; Chan, G. K.-L. Quantum Embedding Theories. *Acc. Chem. Res.* **2016**, *49*, 2705.
- (7) Anderson, P. W. Local Magnetic States in Metals. *Phys. Rev.* **1961**, *124*, 41 – 53.
- (8) Georges, A.; Kotliar, G. Hubbard Model in Infinite Dimensions. *Phys. Rev. B* **1992**, *45*, 6479–6483.
- (9) Georges, A.; Kotliar, G.; Krauth, W.; Rozenberg, M. J. Dynamical Mean-field Theory of Strongly Correlated Fermion Systems and the Limit of Infinite Dimensions. *Rev. Mod. Phys.* **1996**, *68*, 13–125.
- (10) Kotliar, G.; Savrasov, S. Y.; Haule, K.; Oudovenko, V. S.; Parcollet, O.; Marianetti, C. A. Electronic Structure Calculations with Dynamical Mean-field Theory. *Rev. Mod. Phys.* **2006**, *78*, 865.
- (11) Held, K. Electronic structure calculations using dynamical mean field theory. *Adv. Phys.* **2007**, *56*, 829–926.
- (12) Maier, T.; Jarell, M.; Pruschke, T.; Hettler, M. H. Quantum Cluster Theories. *Rev. Mod. Phys.* **2005**, *77*, 1027 – 1080.
- (13) Potthoff, M. Self-Energy-Functional Approach to Systems of Correlated Electrons. *Eur. Phys. J. B* **2003**, *32*, 429.
- (14) Sénéchal, D. An Introduction to Quantum Cluster Methods. *arXiv: 0806.2690 [cond-mat]* **2008**,

- (15) Kananenka, A. A.; Gull, E.; Zgid, D. Systematically Improvable Multiscale Solver for Correlated Electron Systems. *Phys. Rev. B* **2015**, *91*, 121111.
- (16) Rusakov, A. A.; Iskakov, S.; Tran, L. N.; Zgid, D. Self-Energy Embedding Theory (SEET) for Periodic Systems. *J. Chem. Theory Comput.* **2019**, *15*, 229.
- (17) Biermann, S. Dynamical Screening Effects in Correlated Electron Materials: A Progress Report on Combined Many-Body Perturbation and Dynamical Mean Field Theory: GW+DMFT. *J. Phys. : Condens. Matter* **2014**, *26*, 173202.
- (18) Knizia, G.; Chan, G. K.-L. Density Matrix Embedding: A Simple Alternative to Dynamical Mean-Field Theory. *Phys. Rev. Lett.* **2012**, *109*, 186404.
- (19) Bulik, I. W.; Scuseria, G. E.; Dukelsky, J. Density Matrix Embedding from Broken Symmetry Lattice Mean Fields. *Phys. Rev. B* **2014**, *89*, 035140.
- (20) Chen, Q.; Booth, G. H.; Sharma, S.; Knizia, G.; Chan, G. K.-L. Intermediate and Spin-Liquid Phase of the Half-Filled Honeycomb Hubbard Model. *Phys. Rev. B* **2014**, *89*, 165134.
- (21) Zheng, B.-X.; Chan, G. K.-L. Ground-state Phase Diagram of the Square Lattice Hubbard Model from Density Matrix Embedding Theory. *Phys. Rev. B* **2016**, *93*, 035126.
- (22) Zheng, B.-X.; Kretchmer, J. S.; Shi, H.; Zhang, S.; Chan, G. K.-L. Cluster Size Convergence of the Density Matrix Embedding Theory and Its Dynamical Cluster Formulation: A Study with an Auxiliary-field Quantum Monte Carlo Solver. *Phys. Rev. B* **2017**, *95*, 045103.
- (23) Wesolowski, T.; Warshel, A. Frozen Density Functional Approach for Ab Initio Calculations of Solvated Molecules. *J. Phys. Chem* **1993**, *97*, 8050.
- (24) Goodpaster, J. D.; Ananth, N.; Manby, F. R.; Miller, T. F. Exact Nonadditive Kinetic Potentials for Embedded Density Functional Theory. *J. Chem. Phys.* **2010**, *133*, 084103.

- (25) Huang, C.; Pavone, M.; Carter, E. A. Quantum Mechanical Embedding Theory Based on a Unique Embedding Potential. *J. Chem. Phys.* **2011**, *134*, 154110.
- (26) Libisch, F.; Huang, C.; Carter, E. A. Embedded Correlated Wavefunction Schemes: Theory and Applications. *Acc. Chem. Res.* **2014**, *47*, 2768.
- (27) Jacob, C. R.; Neugebauer, J. Subsystem DensityFunctional Theory. *WIREs Comput. Mol. Sci.* **2014**, *4*, 325.
- (28) Chulhai, D. V.; Goodpaster, J. D. Projection-based Correlated Wave Function in Density Functional Theory Embedding for Periodic Systems. *J. Chem. Theory Comput.* **2018**, *14*, 1928–1942.
- (29) Lee, S. J. R.; Welborn, M.; Manby, F. R.; Miller, T. F. Projection-Based Wavefunction-in-DFT Embedding. *Acc. Chem. Res.* **2019**, *52*, 1359.
- (30) Zhu, T.; de Silva, P.; van Aggelen, H.; Van Voorhis, T. Many-Electron Expansion: A Density Functional Hierarchy for Strongly Correlated Systems. *Phys. Rev. B* **2016**, *93*, 201108.
- (31) Zhu, T.; de Silva, P.; Van Voorhis, T. Implementation of the Many-Pair Expansion for Systematically Improving Density Functional Calculations of Molecules. *J. Chem. Theory Comput.* **2019**, *15*, 1089–1101.
- (32) Fan, Z.; Jie, Q.-l. Cluster Density Matrix Embedding Theory for Quantum Spin Systems. *Phys. Rev. B* **2015**, *91*, 195118.
- (33) Zheng, B.-X.; Chung, C.-M.; Corboz, P.; Ehlers, G.; Qin, M.-P.; Noack, R. M.; Shi, H.; White, S. R.; Zhang, S.; Chan, G. K.-L. Stripe Order in the Underdoped Region of the Two-dimensional Hubbard Model. *Science* **2017**, *358*, 1155–1160.
- (34) Gunst, K.; Wouters, S.; De Baerdemacker, S.; Van Neck, D. Block Product Density

- Matrix Embedding Theory for Strongly Correlated Spin Systems. *Phys. Rev. B* **2017**, *95*, 195127.
- (35) Sandhoefer, B.; Chan, G. K.-L. Density Matrix Embedding Theory for Interacting Electron-phonon Systems. *Phys. Rev. B* **2016**, *94*, 085115.
- (36) Wu, X.; Cui, Z.-H.; Tong, Y.; Lindsey, M.; Chan, G. K.-L.; Lin, L. Projected Density Matrix Embedding Theory with Applications to the Two-Dimensional Hubbard Model. *J. Chem. Phys.* **2019**, *151*, 064108.
- (37) Knizia, G.; Chan, G. K.-L. Density Matrix Embedding: A Strong-Coupling Quantum Embedding Theory. *J. Chem. Theory Comput.* **2013**, *9*, 1428–1432.
- (38) Wouters, S.; Jiménez-Hoyos, C. A.; Sun, Q.; Chan, G. K.-L. A Practical Guide to Density Matrix Embedding Theory in Quantum Chemistry. *J. Chem. Theory Comput.* **2016**, *12*, 2706–2719.
- (39) Fulde, P.; Stoll, H. Dealing With the Exponential Wall in Electronic Structure Calculations. *J. Chem. Phys.* **2017**, *146*, 194107.
- (40) Pham, H. Q.; Bernales, V.; Gagliardi, L. Can Density Matrix Embedding Theory with the Complete Activate Space Self-Consistent Field Solver Describe Single and Double Bond Breaking in Molecular Systems? *J. Chem. Theory Comput.* **2018**, *14*, 1960–1968.
- (41) Bulik, I. W.; Chen, W.; Scuseria, G. E. Electron Correlation in Solids via Density Embedding Theory. *J. Chem. Phys.* **2014**, *141*, 054113.
- (42) Sun, Q.; Berkelbach, T. C.; Blunt, N. S.; Booth, G. H.; Guo, S.; Li, Z.; Liu, J.; McClain, J. D.; Sayfutyarova, E. R.; Sharma, S.; Wouters, S.; Chan, G. K.-L. PySCF: the Python-based Simulations of Chemistry Framework. *WIREs Comput. Mol. Sci.* **2018**, *8*, e1340.

- (43) McClain, J.; Sun, Q.; Chan, G. K.-L.; Berkelbach, T. C. Gaussian-Based Coupled-Cluster Theory for the Ground-State and Band Structure of Solids. *J. Chem. Theory Comput.* **2017**, *13*, 1209–1218.
- (44) Sun, Q.; Berkelbach, T. C.; McClain, J. D.; Chan, G. K.-L. Gaussian and Plane-wave Mixed Density Fitting for Periodic Systems. *J. Chem. Phys.* **2017**, *147*, 164119.
- (45) Pham, H. Q.; Hermes, M. R.; Gagliardi, L. Periodic Electronic Structure Calculations With Density Matrix Embedding Theory. *arXiv preprint arXiv:1909.08783* **2019**,
- (46) Foster, J. M.; Boys, S. F. Canonical Configurational Interaction Procedure. *Rev. Mod. Phys.* **1960**, *32*, 300–302.
- (47) Pipek, J.; Mezey, P. G. A Fast Intrinsic Localization Procedure Applicable for Ab-initio and Semiempirical Linear Combination of Atomic Orbital Wave Functions. *J. Chem. Phys.* **1998**, *90*, 4916.
- (48) Edmiston, C.; Ruedenberg, K. Localized Atomic and Molecular Orbitals. *Rev. Mod. Phys.* **1963**, *35*, 457–464.
- (49) Marzari, N.; Vanderbilt, D. Maximally Localized Generalized Wannier Functions for Composite Energy Bands. *Phys. Rev. B* **1997**, *56*, 12847–12865.
- (50) Marzari, N.; Mostofi, A. A.; Yates, Y. R.; Souza, I.; Vanderbilt, D. Maximally localized Wannier functions: Theory and applications. *Rev. Mod. Phys.* **2012**, *84*, 1419 – 1475.
- (51) Jónsson, E. Ö.; Lehtola, S.; Puska, M.; Jónsson, H. Theory and Applications of Generalized Pipek-Mezey Wannier Functions. *J. Chem. Theory Comput.* **2017**, *13*, 460–474.
- (52) Souza, I.; Marzari, N.; Vanderbilt, D. Maximally Localized Wannier Functions for Entangled Energy Bands. *Phys. Rev. B* **2001**, *65*, 035109.
- (53) Damle, A.; Lin, L. Disentanglement via Entanglement: A Unified Method for Wannier Localization. *Multiscale Model. Simul.* **2018**, *16*, 1392–1410.

- (54) Löwdin, P.-O. On the Non-Orthogonality Problem Connected with the Use of Atomic Wave Functions in the Theory of Molecules and Crystals. *J. Chem. Phys.* **1950**, *18*, 365.
- (55) Sun, Q.; Chan, G. K.-L. Exact and Optimal Quantum Mechanics/Molecular Mechanics Boundaries. *J. Chem. Theory Comput.* **2014**, *10*, 3784.
- (56) Reed, A. E.; Weinstock, R. B.; Weinhold, F. Natural Population Analysis. *J. Chem. Phys.* **1985**, *83*, 735–746.
- (57) Knizia, G. Intrinsic Atomic Orbitals: An Unbiased Bridge between Quantum Theory and Chemical Concepts. *J. Chem. Theory Comput.* **2013**, *9*, 4834–4843.
- (58) Saebø, S.; Pulay, P. Local Treatment of Electron Correlation. *Annu. Rev. Phys. Chem.* **1993**, *44*, 213.
- (59) Motta, M.; Ceperley, D. M.; Chan, G. K.-L.; Gomez, J. A.; Gull, E.; Guo, S.; Jiménez-Hoyos, C. A.; Lan, T. N.; Li, J.; Ma, F.; Millis, A. J.; Prokof'ev, N. V.; Ray, U.; Scuseria, G. E.; Sorella, S.; Stoudenmire, E. M.; Sun, Q.; Tupitsyn, I. S.; White, S. R.; Zgid, D.; Zhang, S. Towards the Solution of the Many-Electron Problem in Real Materials: Equation of State of the Hydrogen Chain with State-of-the-Art Many-Body Methods. *Phys. Rev. X* **2017**, *7*, 031059.
- (60) Whitten, J. L. Coulombic Potential Energy Integrals and Approximations. *J. Chem. Phys.* **1973**, *58*, 4496–4501.
- (61) Savrasov, S. Y.; Kotliar, G.; Abrahams, E. Correlated Electrons in δ -Plutonium within a Dynamical Mean-Field Picture. *Nature* **2001**, *410*, 793.
- (62) Savrasov, S. Y.; Kotliar, G. Spectral Density Functionals for Electronic Structure Calculations. *Phys. Rev. B* **2004**, *65*, 245101.

- (63) Pourovskii, L. V.; Amadon, B.; Biermann, S.; Georges, A. Self-Consistency Over the Charge Density in Dynamical Mean-Field Theory: A Linear Muffin-tin Implementation and Some Physical Implications. *Phys. Rev. B* **2007**, *76*, 235101.
- (64) Park, W.; Millis, A. J.; Marianetti, C. A. Computing Total Energies in Complex Materials Using Charge Self-Consistent DFT + DMFT. *Phys. Rev. B* **2014**, *90*, 235103.
- (65) Li, L. H.; Chen, Y.; Behan, G.; Zhang, H.; Petravic, M.; Glushenkov, A. M. Large-Scale Mechanical Peeling of Boron Nitride Nanosheets by Low-energy Ball Milling. *J. Mater. Chem.* **2011**, *21*, 11862.
- (66) Töbrens, D.; Stüßer, N.; Knorr, K.; Mayer, H.; Lampert, G. E9: The New High-Resolution Neutron Powder Diffractometer at the Berlin Neutron Scattering Center. European Powder Diffraction EPDIC 7. 2001; pp 288–293.
- (67) Cheetham, A. K.; Hope, D. A. O. Magnetic Ordering and Exchange Effects in the Antiferromagnetic Solid Solutions $\text{Mn}_x\text{Ni}_{1-x}\text{O}$. *Phys. Rev. B* **1983**, *27*, 6964.
- (68) Perdew, J. P.; Burke, K.; Ernzerhof, M. Generalized Gradient Approximation Made Simple. *Phys. Rev. Lett.* **1996**, *77*, 3865.
- (69) Goedecker, S.; Teter, M.; Hutter, J. Separable Dual-Space Gaussian Pseudopotentials. *Phys. Rev. B* **1996**, *54*, 1703.
- (70) Hartwigsen, C.; Goedecker, S.; Hutter, J. Relativistic Separable Dual-Space Gaussian Pseudopotentials from H to Rn. *Phys. Rev. B* **1998**, *58*, 3641.
- (71) Vandevondele, J.; Hutter, J. Gaussian Basis Sets for Accurate Calculations on Molecular Systems in Gas and Condensed Phases. *J. Chem. Phys.* **2007**, *127*, 114105.
- (72) Stoychev, G. L.; Auer, A. A.; Neese, F. Automatic Generation of Auxiliary Basis Sets. *J. Chem. Theory Comput.* **2017**, *13*, 554–562.

- (73) Paier, J.; Hirschl, R.; Marsman, M.; Kresse, G. The Perdew-Burke-Ernzerhof Exchange-Correlation Functional Applied to the G2-1 Test Set Using a Plane-wave Basis Set. *J. Chem. Phys.* **2005**, *122*, 234102.
- (74) Sundararaman, R.; Arias, T. Regularization of the Coulomb Singularity in Exact Exchange by Wigner-Seitz Truncated Interactions: Towards Chemical Accuracy in Non-trivial Systems. *Phys. Rev. B* **2013**, *87*, 165122.
- (75) Bartlett, J. R.; Musiał, M. Coupled-Cluster Theory in Quantum Chemistry. *Rev. Mod. Phys.* **2007**, *79*, 291.
- (76) Shavitt, I.; Bartlett, R. J. *Many-Body Methods in Chemistry and Physics: MBPT and Coupled Cluster Theory*; Cambridge University, 2009.
- (77) Gao, Y.; Sun, Q.; Yu, J. M.; Motta, M.; McClain, J.; White, A. F.; Minnich, A. J.; Chan, G. K. Electronic Structure of Bulk Manganese Oxide and Nickel Oxide from Coupled Cluster Theory. *arXiv preprint arXiv:1910.02191* **2019**,
- (78) Zhang, I. Y.; Grüneis, A. Coupled Cluster Theory in Materials Science. *Front. Mater.* **2019**, *6*, 123.
- (79) Gygi, F.; Baldereschi, A. Self-Consistent Hartree-Fock and Screened-Exchange Calculations in Solids: Applications to Silicon. *Phys. Rev. B* **1986**, *34*, 4405.
- (80) Welborn, M.; Tsuchimochi, T.; Van Voorhis, T. Bootstrap Embedding: An Internally Consistent Fragment-Based Method. *J. Chem. Phys.* **2016**, *145*, 074102.
- (81) Ricke, N.; Welborn, M.; Ye, H.-Z.; Van Voorhis, T. Performance of Bootstrap Embedding for Long-Range Interactions and 2D Systems. *Mol. Phys.* **2017**, *115*, 2242.
- (82) Ye, H.-Z.; Ricke, N. D.; Tran, H. K.; Van Voorhis, T. Bootstrap Embedding for Molecules. *J. Chem. Theory Comput.* **2019**, *15*, 4497.

- (83) Murnaghan, F. D. The Compressibility of Media under Extreme Pressures. *Proc. Natl. Acad. Sci. U S A* **1944**, *30*, 244.
- (84) Birch, F. Finite Elastic Strain of Cubic Crystals. *Phys. Rev.* **1947**, *71*, 809.
- (85) Schimka, L.; Harl, J.; Kresse, G. Improved Hybrid Functional for Solids: The HSEsol Functional. *J. Chem. Phys.* **2011**, *134*, 024116.
- (86) Sawatzky, G. A.; Allen, J. W. Magnitude and Origin of the Band Gap in NiO. *Phys. Rev. Lett.* **1984**, *53*, 2339.
- (87) Perdew, J. P.; Yang, W.; Burke, K.; Yang, Z.; Gross, E. K. U.; Scheffler, M.; Scuse-
ria, G. E.; Henderson, T. M.; Zhang, I. Y.; Ruzsinszky, A.; Peng, H.; Sun, J.;
Trushin, E.; Görling, A. Understanding Band Gaps of Solids in Generalized Kohn-
Sham Theory. *Proc. Natl. Acad. Sci. USA* **2017**, *114*, 2801–2806.
- (88) Kümmel, S.; Kronik, L. Orbital-Dependent Density Functionals: Theory and Applica-
tions. *Rev. Mod. Phys.* **2008**, *80*, 3.
- (89) Alperin, A. H. *J. Phys. Soc. Japan Suppl. B* **1962**, *17*, 12.
- (90) Fender, B. E. F.; Jacobson, A. J.; Wedgwood, F. A. Covalency Parameters in MnO,
 α MnS, and NiO. *J. Chem. Phys.* **1968**, *48*, 990.
- (91) Chatterji, T.; McIntyre, G. J.; Lindgard, P.-A. Antiferromagnetic Phase Transition and
Spin Correlations in NiO. *Phys. Rev. B* **2009**, *79*, 172403.
- (92) Germann, K. H.; Maier, K.; Strauß, E. Magnetic Order Induced Birefringence and
Critical Behaviour of the Long Range Order Parameter in NiO. *Solid State Commun.*
1974, *14*, 1309.
- (93) Negovetić, I.; Konstantinović, J. The Critical Behaviour of Spontaneous Magnetization
in the Antiferromagnetic NiO. *Solid State Commun.* **1973**, *13*, 249.

- (94) Zhu, T.; Cui, Z.-H.; Chan, G. K.-L. Efficient Implementation of Ab Initio Quantum Embedding in Periodic Systems: Dynamical Mean-Field Theory. *arXiv:1909.08592* **2019**,

Graphical TOC Entry

